



Strong-coupling superconductivity of the Heusler-type compound ScAu₂Al: *Ab initio* studiesGabriel Kuderowicz  and Bartłomiej Wiendlocha 

AGH University of Krakow, Faculty of Physics and Applied Computer Science, Aleja Mickiewicza 30, 30-059 Krakow, Poland



(Received 6 July 2023; revised 8 October 2023; accepted 15 November 2023; published 1 December 2023)

The ScAu₂Al superconducting Heusler-type compound was recently characterized to have the highest critical temperature of $T_c = 5.12$ K and the strongest electron-phonon coupling among the Heusler family. In this work, the electronic structure, phonons, electron-phonon coupling, and superconductivity of ScAu₂Al are studied using *ab initio* calculations. The spin-orbit coupling significantly changes the electronic structure removing the van Hove singularity from the vicinity of the Fermi level. In the phonon spectrum, low-frequency acoustic modes, additionally softened by the spin-orbit interaction, strongly couple with electrons, leading to the electron-phonon coupling constant $\lambda = 1.25$, a record high among Heuslers. The density functional theory for superconductors is then used to analyze superconducting state in this two-band superconductor. The effect of spin fluctuations (SF) on superconductivity is also analyzed. The calculated critical temperatures of $T_c = 5.16$ K (4.79 K with SF) agree very well with the experiment, confirming the electron-phonon mechanism of superconductivity and showing a weak spin-fluctuation effect. The superconducting gaps formed on two Fermi surface sheets exhibit moderate anisotropy. Their magnitudes confirm the strong coupling regime, as the reduced average values are $2\Delta_{b_1}/k_B T_c \simeq 4.1$ and $2\Delta_{b_2}/k_B T_c \simeq 4.3$. Anisotropy of the gaps and large spread in their values significantly affect the calculated quasiparticle density of states.

DOI: [10.1103/PhysRevB.108.224501](https://doi.org/10.1103/PhysRevB.108.224501)**I. INTRODUCTION**

Heusler family of compounds consists of more than a thousand systems with a wide variety of physical properties. To name a few, one can find half-metallic ferromagnetism [1–10], shape memory effect [11,12], heavy fermion behavior [13–17], charge density waves [18], topologically nontrivial states [19–23], and superconductivity [24–29]. In many cases, the properties of Heusler compounds can be easily tuned by chemical substitution [4,30–32] or pressure [33,34]. These intermetallic materials have a general formula XY₂Z for the so-called full Heusler compounds and XYZ for their half-Heusler counterparts. The full Heusler compounds crystallize in a cubic structure with a space group $Fm-3m$, No. 225, shown in Fig. 1. The relative simplicity of the structure and the wealth of physical properties make this family a very active and compelling field of research.

To our knowledge, to date superconductivity has been reported in 34 full Heusler compounds [29]. Generally, they follow Matthias' rule, which states that the maximum superconducting transition temperature T_c is expected for 5 to 7 valence electrons per atom in the unit cell [35,36]. The highest T_c among Heusler compounds was recently reported to be 5.12 K in ScAu₂Al [37] which has 7 electrons per atom (28 per formula unit). However, a considerably lower $T_c = 4.4$ K was previously reported for that system [29,38,39]. Moreover, on the basis of the McMillan formula [40], measured Debye temperature ($\theta_D = 180$ K) and using a Coulomb pseudopotential value of $\mu^* = 0.13$ Bag *et al.* [37] estimated the

electron-phonon coupling constant to be $\lambda = 0.77$, suggesting a moderate strength of the electron-phonon interaction, not necessarily expected for a case with the highest T_c in this family of materials.

This raises the question of whether strongly coupled superconductivity with $\lambda > 1.0$ actually exists among Heuslers. In other intermetallic superconducting families, such as Laves phases or A-15 compounds, materials with the highest T_c s exhibit $\lambda > 1.0$, for example, SrIr₂ ($\lambda = 1.1$, $T_c = 6.1$ K) [41], CaIr₂ ($\lambda = 1.05$, $T_c = 7$ K) [42,43], or Nb₃Ge ($\lambda \simeq 1.7$, $T_c = 21.8$ K) [44]. Therefore it is worth considering whether the Heusler family is in some way “distinct” and incapable of achieving higher values of λ than the postulated ~ 0.8 , or the estimation of λ based on the McMillan formula provides a very inaccurate result. These facts served as motivation for the undertaking of theoretical studies for ScAu₂Al.

This work provides a theoretical analysis of superconductivity in ScAu₂Al to determine the electron-phonon coupling strength, critical temperature, and the structure and anisotropy of the superconducting gap. Calculations will help verify the strong- or moderate-coupling regime of superconductivity and to determine which of the experimentally reported values of T_c corresponds to the one for the ideal ScAu₂Al phase, as due to the presence of defects and disorder, frequently observed in Heuslers, the discrepancy in experimental T_c 's is not unusual. Using the *ab initio* methods, we calculate the electronic structure, phonons, and electron-phonon coupling functions using density functional theory (DFT). To investigate the anisotropy of the superconducting gap and obtain the critical temperature without using any external parameters, the density functional theory for superconductors (SCDFT) in the decoupling approximation [45–48] is used. In these

*wiendlocha@fis.agh.edu.pl

calculations, we avoid the need to assume the value of the effective Coulomb repulsion parameter μ^* present in McMillan [40] or Allen-Dynes [49] T_c formulas, and the ferromagnetic spin-fluctuation effect, competing with superconductivity, can be analyzed.

The main results of our calculations show that ScAu_2Al is a two-band strong-coupled electron-phonon superconductor with $\lambda \sim 1.3$ significantly increased by the spin-orbit coupling, $T_c \simeq 5$ K and $2\Delta/k_B T_c \simeq 4.1$, with a moderate anisotropy of the two superconducting gaps.

II. COMPUTATIONAL DETAILS

DFT calculations were performed using the QUANTUM ESPRESSO package [50,51]. Projected augmented wave (PAW) pseudopotentials from the PSLibrary [52,53] were used, with the Perdew-Burke-Ernzerhof exchange correlation functional [54]. The effects of spin-orbit coupling (SOC) were studied by performing the scalar-relativistic and full-relativistic calculations. Self-consistent calculations were done on a $12 \times 12 \times 12$ Monkhorst-Pack \mathbf{k} -point mesh. Electronic density of states (DOS) and eigenvalues for electron-phonon matrix elements were obtained on a $24 \times 24 \times 24$ grid, whereas the Fermi surface (FS) was rendered from a $48 \times 48 \times 48$ grid. Kinetic energy cutoffs in the plane wave expansion of wave functions and charge density were set to 100 and 600 Ry, respectively. In phonon calculations, dynamical matrices were calculated for a $6 \times 6 \times 6$ \mathbf{q} -point grid which corresponds to 16 inequivalent \mathbf{q} points, from which the interatomic force constants in real space were calculated using Fourier interpolation methods. In Ref. [55], we show that these \mathbf{k} - and \mathbf{q} -point samplings were sufficient to obtain convergent results and discuss convergence against smearing parameters of the cold-smearing technique, used during integrations. In addition, a comparison of the electronic structure obtained in the pseudopotential calculations and from the full-potential all-electron linearized augmented plane wave method, implemented in the WIEN2K package [56,57], is shown [55], which validates the choice of pseudopotentials.

Superconducting density functional theory (SCDFT) calculations were carried out using the Superconducting Toolkit (SCTK) [48] which is interfaced with QUANTUM ESPRESSO. As this procedure requires a shifted \mathbf{q} -point mesh, the prerequisite electron-phonon calculations were repeated on a shifted $6 \times 6 \times 6$ \mathbf{q} -point grid, containing 28 independent points, with the $12 \times 12 \times 12$ and $24 \times 24 \times 24$ \mathbf{k} -point meshes for self-consistent cycle and eigenvalues calculations. Here, all integrations are done using the tetrahedron method.

The volume of the unit cell was relaxed with the Broyden-Fletcher-Goldfarb-Shanno algorithm. The obtained lattice constants, 6.5894 Å without SOC and 6.5775 Å with SOC, are slightly larger than the experimental one, equal to 6.5305 Å [37]. Such an overestimation is typical for the GGA exchange correlation functional.

III. RESULTS AND DISCUSSION

A. Electronic structure

The calculated electronic dispersion relations and the Fermi surface of ScAu_2Al are shown in Fig. 2, and the

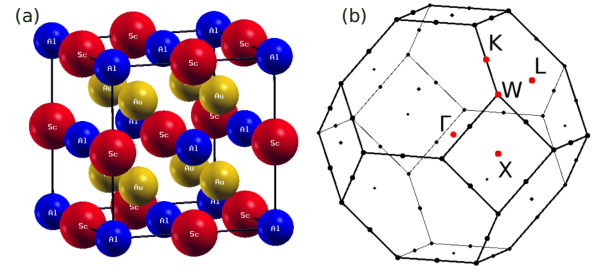


FIG. 1. (a) Unit cell of the ScAu_2Al full Heusler compound with interpenetrating fcc sublattices; (b) Brillouin zone with high-symmetry points.

densities of states (DOS) in Fig. 3. Brillouin zone with the high-symmetry points is shown in Fig. 1(b). In general, our results agree well with the earlier band-structure calculations [37,59].

Two bands cross the Fermi level building two Fermi surface sheets [Figs. 2(c) and 2(d)]: one, hole-like, with a shape of a cube skeleton stretched between the L points, and the second, electron-like, with large pockets centered at X and small pockets around K . The first Fermi surface sheet, shown in Fig. 2(c), contributes approximately 75% of the total density of states at the Fermi level, $N(E_F)$, as electrons have a lower Fermi velocity compared to the second sheet.

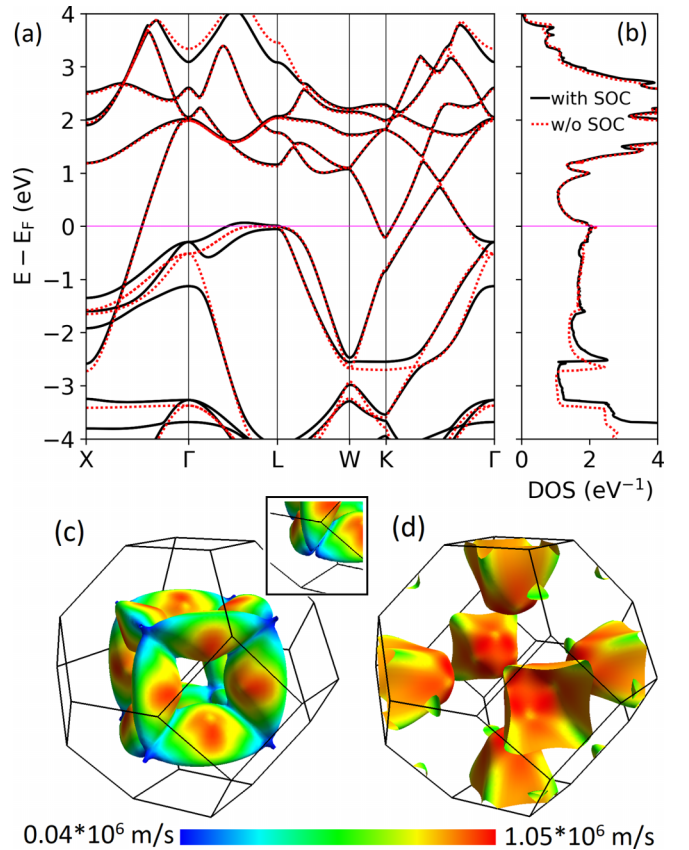


FIG. 2. (a) Electronic bands and (b) total DOS of ScAu_2Al . [(c) and (d)] Fermi surface with SOC and colored with the Fermi velocity. Inset shows a fragment near the L point calculated without SOC. FS was visualized in FERMISURFER [58].

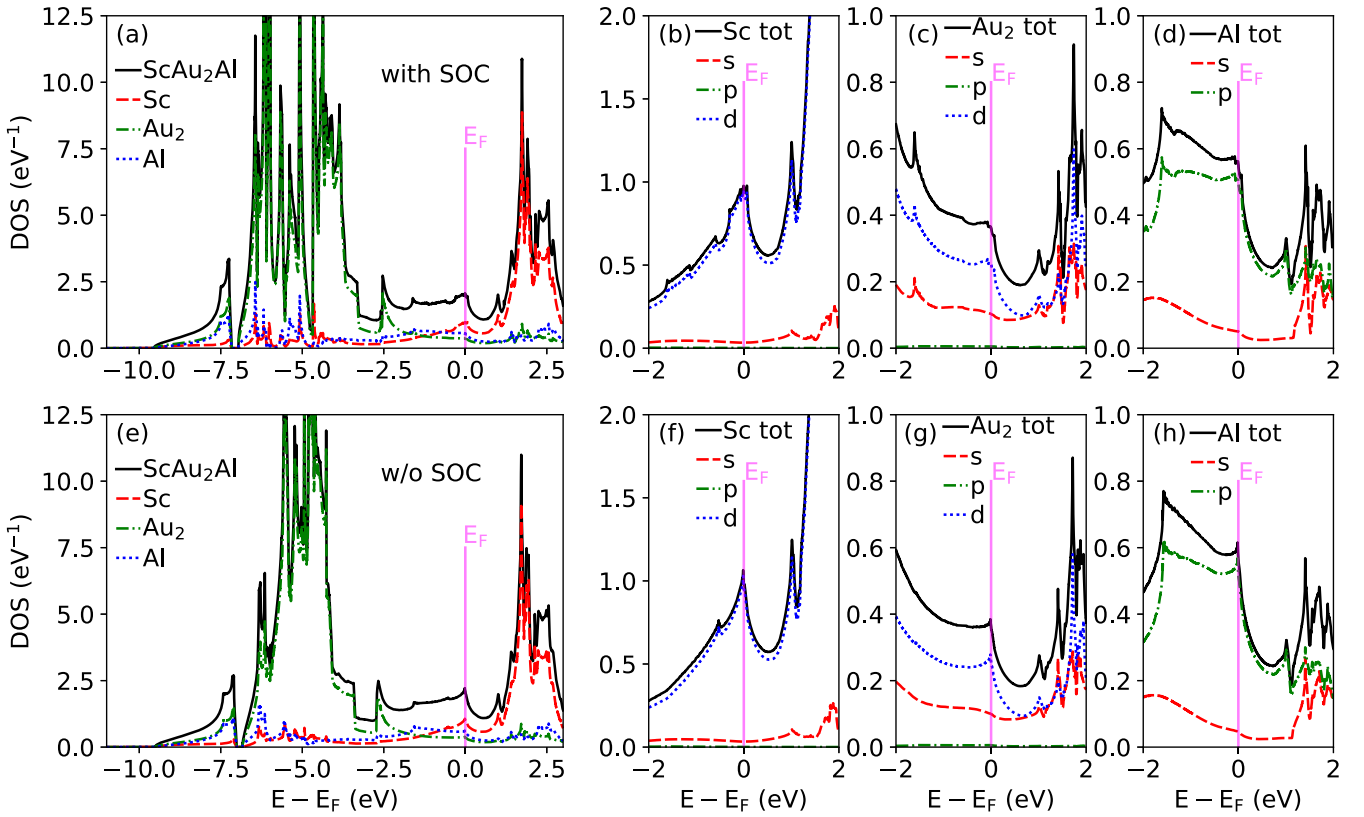


FIG. 3. Total and projected density of states (DOS) of ScAu_2Al . Top panels show the full-relativistic results, bottom with SOC neglected. In (c) and (g), the densities of states are plotted for two Au atoms, the single-atomic orbital contribution is two times smaller.

The first notable feature in the electronic structure is a flat band near the L point, located at the Fermi energy E_F in the scalar-relativistic case. Because the derivative $\nabla E(k)$ approaches zero, a van Hove singularity appears in the DOS as a sharp kink at E_F in Figs. 3(e)–3(h). The inset in Fig. 2 shows a piece of the Fermi surface near the L point, calculated without SOC. As one can see, there are no states exactly at the L point and a closer analysis shows that, in fact, the electronic band is located 10 meV below E_F .

Spin-orbit coupling visibly affects bands near the Fermi level in the Γ - L direction, removing the band degeneracy. Two flat bands are moved away from the Fermi energy, removing the van Hove singularity from the vicinity of E_F . This results in the formation of two DOS peaks that merge into a broader maximum visible in Figs. 3(a)–3(d), with slightly decreased $N(E_F)$, whereas in the Fermi surface small tubes around L are built, connecting the FS fragments [Fig. 2(c)].

A more detailed view of the band structure is shown in Fig. 4 where the bands are colored according to their orbital character.

A dominant contribution of Sc- d states is noticeable, especially in the flat-band region and for a linear band between K and Γ . In the Γ - L direction, SOC pushes Sc- $d_{j_{5/2}}$ below E_F , leaving the dominant contribution to Sc- $d_{j_{3/2}}$. The contributions from the Au- d and Al- p states, compared to Sc, are more uniformly distributed between the bands and as a function of the distance from E_F .

Analysis of densities of states in Fig. 3 confirms that the states at E_F are mainly built from Sc- $3d$, and the next contribution comes from Al- $3p$ orbitals. Although the two Au atoms contribute 22 of 28 valence electrons in the ScAu_2Al unit cell, their almost filled $5d$ shells form bands deep below E_F . The total and projected values of $N(E_F)$ are collected in Table I and the largest contribution to DOS at the Fermi level comes from scandium.

Although spin-orbit coupling visibly affects the band structure near E_F , it has a small effect on the magnitude of $N(E_F)$. The relativistic value is only about 2% smaller than the scalar-relativistic one. The calculated density of states (with SOC) gives the electronic specific heat coefficient $\gamma_{\text{band}} = 4.74 \text{ mJ}/(\text{mol K}^2)$. The experimental Sommerfeld coefficient, reported in [37] is $\gamma_{\text{expt}} = 6.75 \text{ mJ}/(\text{mol K}^2)$. That gives the electron phonon renormalization factor $\lambda_\gamma = \gamma_{\text{expt}}/\gamma_{\text{band}} - 1 = 0.425$, which is very small considering the high $T_c =$

TABLE I. Calculated total and projected $N(E_F)$ of ScAu_2Al , and bandstructure values of the Sommerfeld coefficient γ_{band} .

	$N(E_F)$ (eV^{-1})				γ_{band} ($\frac{\text{mJ}}{\text{mol K}^2}$)
	total	Sc	Au ₂	Al	
with SOC	2.010	0.972	0.362	0.556	4.74
w/o SOC	2.043	0.990	0.359	0.565	4.82

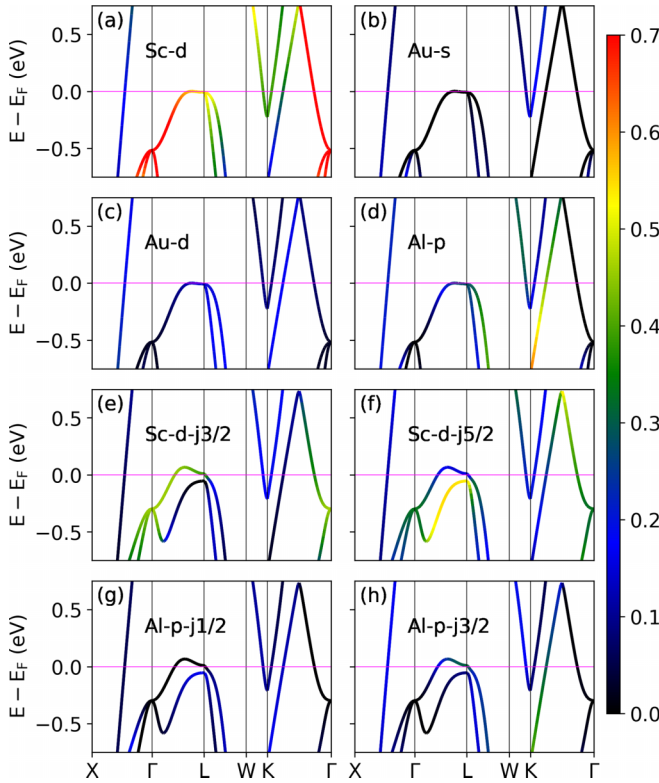


FIG. 4. Electronic bands colored according to their orbital character. (a)–(d) show the scalar-relativistic results, whereas in (e)–(h), spin-orbit coupling is included.

5.12 K. However, we consider the reported value of $\gamma_{\text{expt}} = 6.75 \text{ mJ}/(\text{mol K}^2)$ as unlikely. The value of γ_{expt} was obtained in Ref. [37] by fitting the data of $C_p(T)$ measured in a magnetic field of 10 kOe to the standard equation $C_p/T = \gamma + \beta T^2 + \delta T^4$. Measurements were reported for the temperature range 2–5.5 K; the fit range was not reported. In Ref. [55], we reanalyze the specific heat data from [37], performing a set of fits in the temperature range 2.0 K – T_{max} , with 4.5 K < T_{max} < 5.5 K (T_{max}^2 from 20 to 30 K²). It appeared that the obtained γ is very sensitive to the fit range; it varies from 12 mJ/(mol K²) for the narrower fit range to 2.8 mJ/(mol K²) for the broader, while it should be constant within some error bar. Similar situation holds for the Debye temperature, obtained from this fit. The problem in stabilization of the temperature, mentioned in Ref. [37], could have influenced the measurements; however, as we discuss in Ref. [55] in temperatures above 2 K the lattice specific heat in ScAu₂Al cannot be analyzed using the Debye $C = \beta T^3 + \delta T^5$ formula, due to the presence of low-frequency phonon mode, discussed in the next paragraph. To precisely determine the Sommerfeld parameter and limit the influence of the lattice contribution, specific heat should be measured at lower temperatures, below 2 K. Our theoretical value of the Sommerfeld parameter, renormalized by the calculated electron-phonon coupling constant (see the following sections), points to the value of $\gamma \sim 11 \text{ mJ}/(\text{mol K}^2)$. Clearly, the specific heat in ScAu₂Al requires further experimental low-temperature studies to provide conclusive results and comparison.

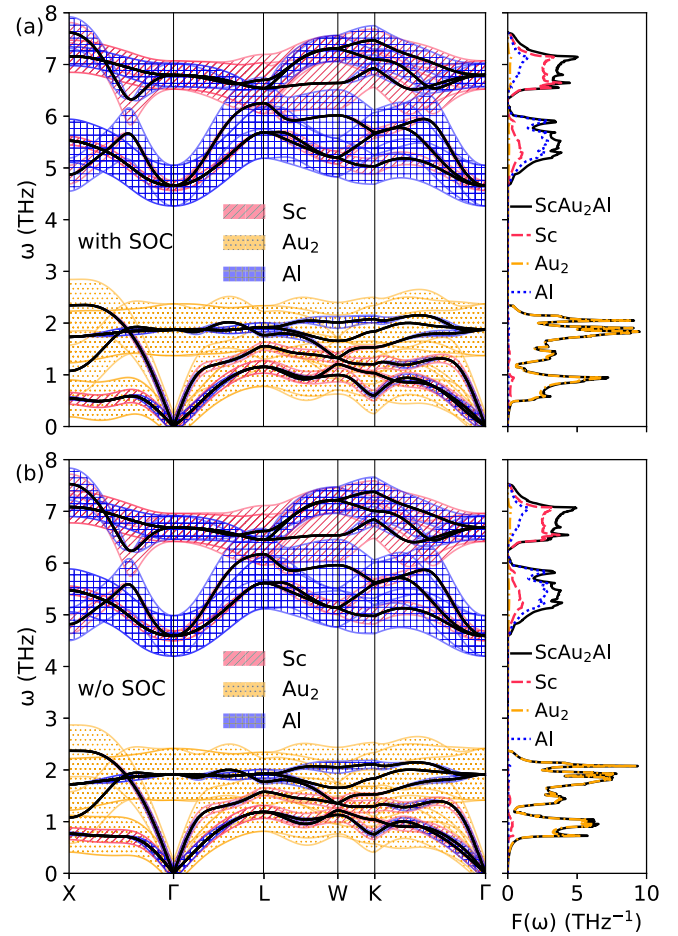


FIG. 5. Phonon bands and partial phonon density of states of ScAu₂Al. Color shading with hatches represents atomic contributions to phonon branches.

B. Phonons

Figure 5 presents the phonon dispersion relations $\omega_{\mathbf{q},\nu}$ and the phonon density of states $F(\omega)$. Gold, as expected for the heaviest atom, constitutes mostly the first six phonon modes with the lowest frequency, up to about 2.5 THz. These phonon branches have minor contributions from scandium and aluminum. A large gap in the phonon spectrum is formed, as the next phonons appear around 5 THz. Such a separation of phonon modes is expected because Au atoms are approximately 8 and 4 times heavier than Al and Sc atoms, respectively. The higher-frequency part of the phonon spectrum, involving Sc and Al vibrations, span the range from 5 THz to about 7.5 THz and is grouped into two parts. Three phonon modes, between roughly 5 and 6 THz, have a dominant Al character, whereas the highest three modes describe mostly the vibrations of Sc. Thus inversion of the phonon modes is noticed, because despite the fact that Sc is 67% heavier than Al, its phonon modes have much higher frequencies. This inversion is caused by the stronger bonding of scandium atoms inside the structure, which leads to higher values of the force constants matrix elements. For example, the restoring force acting on Sc when it is displaced in the x direction is about two times greater than for Al and Au, and the force constant

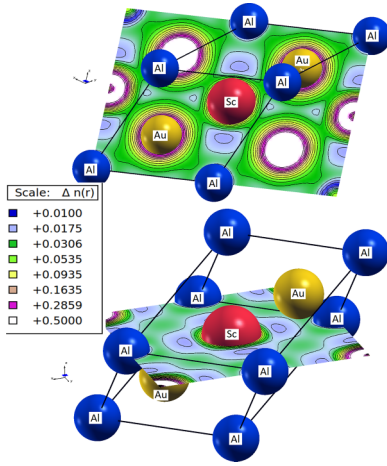


FIG. 6. Electron density (number of electrons/ a_B^3 , where a_B is the Bohr radius) in the primitive cell of ScAu_2Al . The electron density was visualized using XCRYSDEN [60].

matrix elements for the Sc-Au nearest-neighbor pair are approximately three times greater than those for the Al-Au pair. This is supported by the charge density distribution, shown in Fig. 6 in the Al-Sc-Au and Sc-Al planes. The electron density between Sc and Au is generally larger than that between the Al and Au or Al and Sc pairs. This gives a larger metallic contribution to the mixed metallic-ionic bonding in this structure, strengthening the bonding between Sc and Au, compared to Al-Au or Al-Sc. In turn, higher values of the force constants result in higher frequencies of Sc vibrations, above Al.

Taking a closer look at the low-frequency range, we notice a strong softening of the first two acoustic modes, especially in the Γ -X direction and at the K point. All three atom species make a visible contribution to these modes near the X point. On the other hand, the third acoustic mode at the X point has almost zero contribution from Sc and Al vibrations. SOC further enhances this softening as highlighted in Fig. 7, therefore, it must be included to accurately analyze superconductivity in ScAu_2Al , since the low-frequency phonon modes give the largest contribution to the electron-phonon coupling

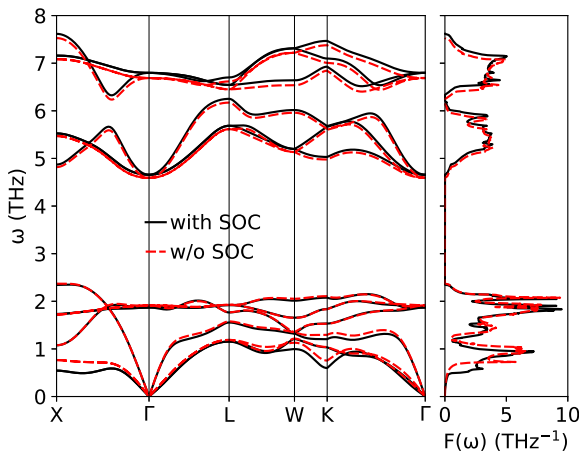


FIG. 7. Effect of spin-orbit coupling on the phonon dispersion relations and phonon density of states of ScAu_2Al .

parameter λ . As far as the optical modes are concerned, the SOC slightly increases the phonon frequencies of the upper optical branches, which can be attributed to a slightly stiffened lattice because the lattice parameter computed with SOC is smaller than the scalar-relativistic one. The average phonon frequencies are 3.82 THz (with SOC) and 3.80 THz (without SOC).

One of the possible reasons for the softening of phonons in metals is the Kohn anomaly, which occurs if large fragments of the Fermi surface can be connected by a single vector \mathbf{q} (FS exhibits strong nesting). In the case of ScAu_2Al , the phonon branches in Γ -X gradually flatten, so there are no sharp dips in the dispersion relation, indicating a characteristic discontinuity of a derivative of $\omega(\mathbf{q})$. To quantitatively investigate the nesting of the Fermi surface, we calculated the values of the nesting function

$$\chi(\mathbf{q}) = \sum_{n,n'} \int_{\text{BZ}} \frac{d^3\mathbf{k}}{V_{\text{BZ}}} \delta(E_F - E_{n,\mathbf{k}}) \delta(E_F - E_{n',\mathbf{k}+\mathbf{q}}). \quad (1)$$

Figure 8(a) shows $\chi(\mathbf{q})$ calculated in selected directions in the Brillouin zone. The largest number of states are connected by vectors starting from the first band, which builds the FS sheet shown in Fig. 2(c) and has large contributions from Sc- d - $j_{3/2}$. Apart from the irrelevant peak in Γ , the nesting function is strongly enhanced in the Γ -X direction and near the X point, which is correlated with the observed softening of the first acoustic phonon mode. Furthermore, $\chi(\mathbf{q})$ is enhanced at the K point, where we also noticed softened phonons. Nesting vectors Γ -X and Γ -K are visualized on the Fermi surface in Figs. 8(c) and 8(e), respectively. Furthermore, spin-orbit coupling significantly increases $\chi(\mathbf{q})$ in the Γ -X direction, as shown in Figs. 8(a) and 8(b), which partly answers the question why the Γ -X acoustic mode is additionally softened in the relativistic case. Analysis of $\chi(\mathbf{q})$ shows that the specific geometry of the Fermi surface is beneficial for strong electron-phonon coupling and superconductivity in ScAu_2Al .

To further investigate the character of the softened phonon mode in Γ -X, we visualized the movement of the atoms in the real space for the phonons at the X point in Fig. 9. This also allows one to see the additional difference imposed by spin-orbit coupling, as SOC increases the $\chi(\mathbf{q})$ values in the Γ -X direction, but also modifies the atomic displacement, leading to a much more softened phonon mode in the fully relativistic case, compared to the scalar-relativistic one. What we can observe is that without SOC in the first two degenerate modes, every atom moves along the diagonal of the base of the unit cell, in the direction where all atoms are aligned. Spin-orbit coupling by influencing the electronic structure, charge densities, and force constants, qualitatively changes this movement pattern because then both Au atoms vibrate in a direction at an angle approximately 130° to the one of Sc and Al, in a less dense-packed direction. This results in a lowering of the vibration frequency. The last acoustic mode at the X points consists only of Au vibrations, and neither its frequency nor the normal mode eigenvectors are visibly affected by the SOC. In Ref. [55] animations of the lowest-frequency phonon modes at X , W , K , L and the middle of X - Γ are additionally provided. It is interesting to note that at the W point Au atoms move in circles, so the investiga-

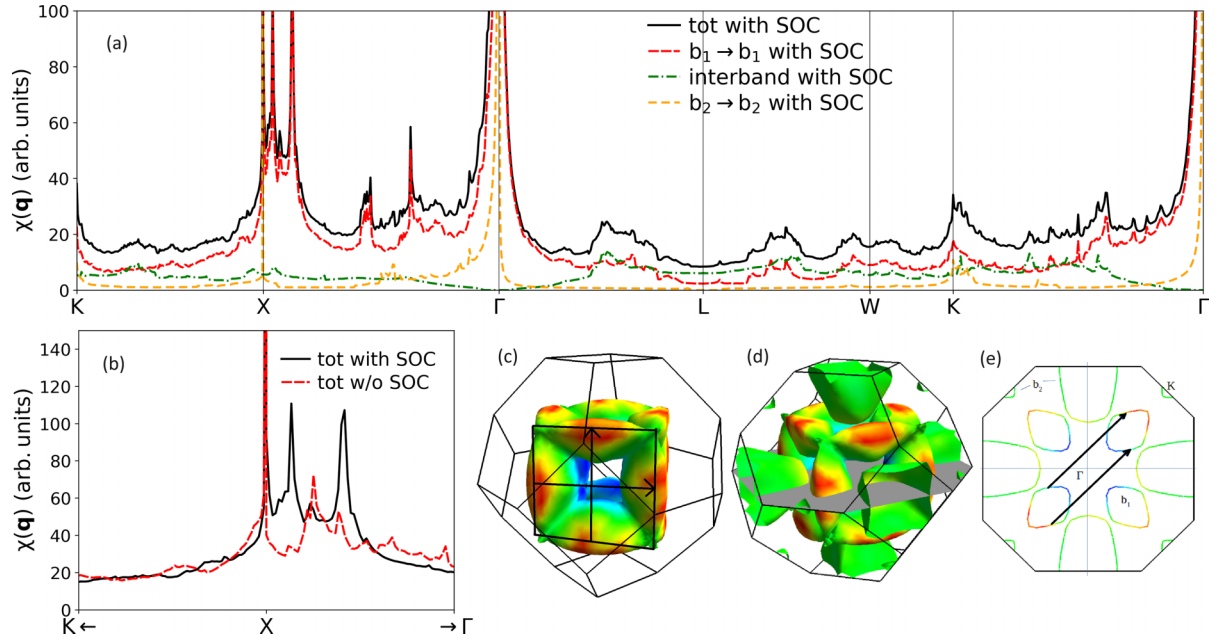


FIG. 8. (a) Nesting function of ScAu_2Al with separated contributions from bands (see text), labels “ b_1 ” and “ b_2 ” refer to bands 1 and 2; (b) zoom near the X point; (c) nesting vectors parallel to Γ - X ; and (d) FS cut on which nesting vectors, parallel to Γ - K , are plotted in (e). Fermi surface is colored with electron-phonon coupling constant calculated using SCDFE (see Sec. III D).

tion of the chirality of phonons [61–63] in ScAu_2Al may be potentially interesting. Furthermore, SOC also causes a circular trajectory of Au movement in the point in the middle of X - Γ , further highlighting that SOC substantially changes

the vibrational properties of ScAu_2Al . Chiral phonon effects would be especially interesting if it were possible to break the time-reversal and inversion symmetries of the structure by synthesizing a noncentrosymmetric half-Heusler analog with magnetic dopants. In such a case, an overall phonon angular momentum, carried by individual chiral modes, does not vanish, and this could be a possible interesting point for further studies on related Heusler structures.

C. Electron-phonon coupling

Electron-phonon interaction is described by the hamiltonian [64–66]

$$\hat{H} = \sum_{\mathbf{k}, \mathbf{q}, v, i, j} g_{\mathbf{q}}^v(\mathbf{k}, i, j) c_{\mathbf{k}+\mathbf{q}}^{\dagger i} c_{\mathbf{k}}^j (b_{-\mathbf{q}}^{\dagger v} + b_{\mathbf{q}}^v). \quad (2)$$

Operators c refer to electrons and b to phonons, with lower indices describing wave vectors and upper band numbers (\mathbf{q} and v for phonons and \mathbf{k}, i, j , for electrons). The matrix element $g_{\mathbf{q}}^v(\mathbf{k}, i, j)$ has a form [66]

$$g_{\mathbf{q}}^v(\mathbf{k}, i, j) = \sum_s \left(\frac{\hbar}{2M_s \omega_{\mathbf{q}v}} \right)^{1/2} \langle \psi_{i, \mathbf{k}} | \frac{dV_{scf}}{d\hat{u}_{v,s}} \cdot \hat{\epsilon}_v | \psi_{j, \mathbf{k}+\mathbf{q}} \rangle, \quad (3)$$

where index s labels atoms in the unit cell, $\psi_{i, \mathbf{k}}$ is an electronic wavefunction, $\frac{dV_{scf}}{d\hat{u}_{v,s}}$ is a self-consistently calculated change in the electronic potential caused by displacing atom in the direction $\hat{u}_{v,s}$ and $\hat{\epsilon}_v$ is a phonon polarization vector. Then one can introduce the phonon linewidth [67]

$$\gamma_{\mathbf{q}}^v = 2\pi \omega_{\mathbf{q}v} \sum_{ij} \int \frac{d^3k}{\Omega_{BZ}} |g_{\mathbf{q}}^v(\mathbf{k}, i, j)|^2 \times \delta(E_{\mathbf{q}}^i - E_F) \delta(E_{\mathbf{k}+\mathbf{q}}^j - E_F). \quad (4)$$

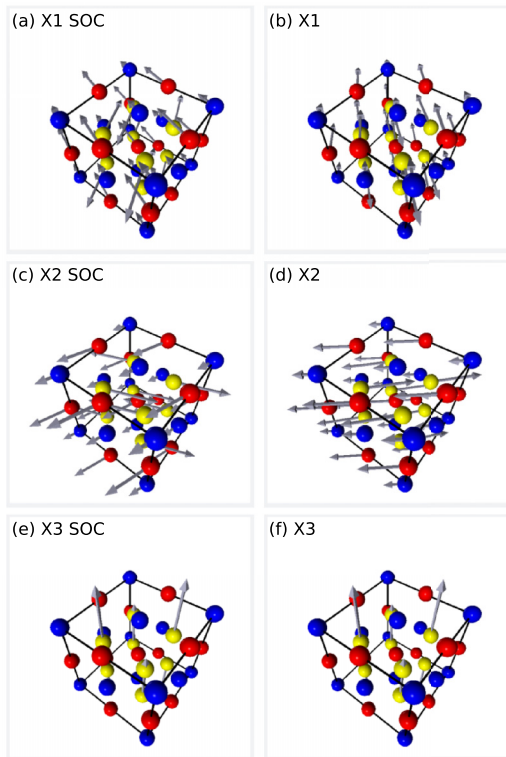


FIG. 9. Acoustic phonon modes at $X = (0, 1, 0)$ in the unit cell of ScAu_2Al . Sc, Au, and Al atoms are colored red, yellow and blue, respectively.

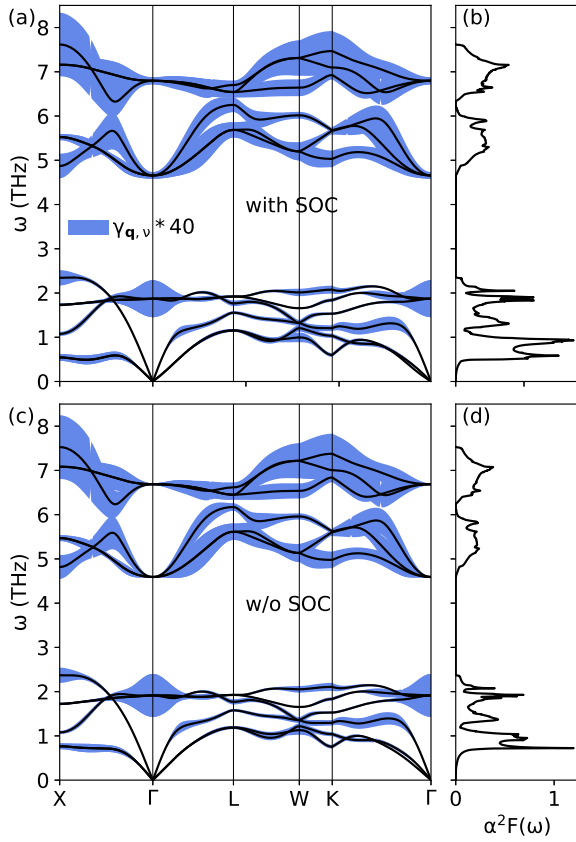


FIG. 10. Phonon linewidths multiplied by 40 and Eliashberg functions of ScAu_2Al .

It is worth noting that phonon linewidths do not directly depend on the phonon frequencies, thus they play a role of electronic contributions to the electron-phonon interaction. Dirac deltas select only electrons from the Fermi surface to participate in the electron-phonon interaction, and the matrix element g is the coupling strength. The phonon linewidth is inversely proportional to the phonon's lifetime. Now one can define the Eliashberg function

$$\alpha^2 F(\omega) = \frac{1}{2\pi N(E_F)} \sum_{\mathbf{q}\nu} \delta(\omega - \omega_{\mathbf{q}\nu}) \frac{\gamma_{\mathbf{q}\nu}}{\hbar\omega_{\mathbf{q}\nu}} \quad (5)$$

and the electron-phonon coupling constant

$$\lambda = 2 \int_0^{\omega_{\max}} \frac{\alpha^2 F(\omega)}{\omega} d\omega. \quad (6)$$

A more detailed discussion can be found in [64].

Figure 10 shows the phonon linewidths plotted over the dispersion relations and the Eliashberg function. Typically, $\gamma_{\mathbf{q}\nu}^v$ is small for acoustic modes, but here it is pronounced in the softened branch in the Γ - X direction. Because the Eliashberg function is inversely proportional to the phonon frequency, the contribution of the lowest mode enhances $\alpha^2 F(\omega)$. It is well seen in Fig. 11 where the Eliashberg function is plotted together with the phonon density of states $F(\omega)$. Furthermore, since the electron-phonon coupling constant λ is proportional to $\alpha^2 F(\omega)/\omega$, the contribution of the softened mode will be the largest. The cumulative frequency distribution of $\lambda(\omega)$,

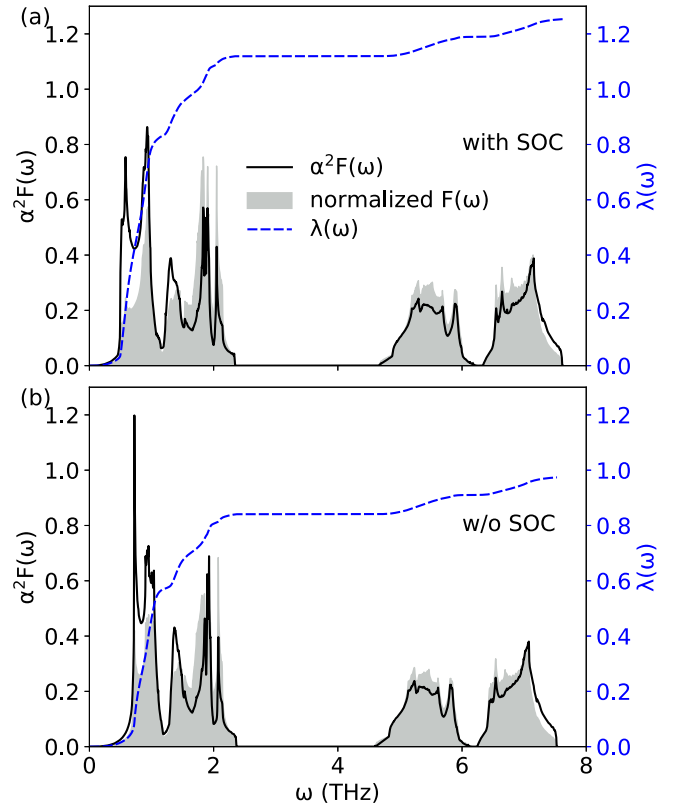


FIG. 11. Eliashberg functions, normalized phonon density of states and cumulative electron-phonon coupling constant.

calculated by integrating equation (6) up to the frequency ω , is shown in Fig. 11. The dominant role of the low-frequency Au-dominated modes (below 2.33 THz) in contributing to the electron-phonon coupling in ScAu_2Al is very well seen. They contribute approximately 86% of λ in the scalar-relativistic case, and the spin-orbit coupling increases this to 89%.

The scalar-relativistic electron-phonon coupling constant is $\lambda = 0.97$ and is remarkably enhanced in about 30%, to $\lambda = 1.25$, when spin-orbit coupling is included. The contributions λ_ν from the each of the phonon modes ν are collected in Table II. Analyzing these values, one can conclude that the relativistic increase of λ is mostly contributed by the two lowest acoustic phonon modes, as λ_1 increases from 0.295 to 0.453 and λ_2 from 0.266 to 0.368.

To analyze whether this increase of λ due to SOC is more related to the increase in the interaction strength (via the phonon linewidths) or due to decrease of phonon frequencies, we have calculated values of two integrals

$$I = \int_0^{\omega_{\max}} \omega \cdot \alpha^2 F(\omega) d\omega, \quad (7)$$

$$\langle \omega^2 \rangle = \int_0^{\omega_{\max}} \omega \cdot \alpha^2 F(\omega) d\omega \Big/ \int_0^{\omega_{\max}} \alpha^2 F(\omega) \frac{d\omega}{\omega}. \quad (8)$$

The integral I is a frequency-independent measure of electronic contribution to λ [41,68], and $\langle \omega^2 \rangle$ is defined in such

TABLE II. Parameters of the electron-phonon interaction in ScAu₂Al for the total phonon spectrum and individual phonon modes: the electron-phonon coupling parameter λ [Eq. (6)], the frequency-independent electronic contribution I [Eq. (7)], and average square frequency $\langle\omega^2\rangle$ [Eq. (8)].

	total	value for the phonon mode no.											
		1	2	3	4	5	6	7	8	9	10	11	12
λ													
with SOC	1.253	0.453	0.368	0.143	0.059	0.049	0.047	0.026	0.023	0.022	0.018	0.021	0.025
w/o SOC	0.974	0.295	0.266	0.128	0.056	0.048	0.047	0.025	0.023	0.021	0.017	0.021	0.025
I (THz ²)													
with SOC	3.229	0.118	0.111	0.130	0.087	0.085	0.102	0.346	0.333	0.362	0.396	0.510	0.649
w/o SOC	3.122	0.103	0.106	0.124	0.084	0.084	0.102	0.336	0.326	0.345	0.376	0.498	0.638
$\langle\omega^2\rangle$ (THz ²)													
with SOC	5.153	0.520	0.605	1.815	2.949	3.466	4.287	27.081	29.294	33.060	44.624	48.701	51.781
w/o SOC	6.411	0.701	0.794	1.939	2.989	3.506	4.349	26.431	28.592	32.365	43.397	47.482	50.522

a way that $\lambda = \frac{2I}{\langle\omega^2\rangle}$.¹ For the whole phonon spectrum, the values are $I = 3.229$ THz², $\langle\omega^2\rangle = 5.153$ THz² (with SOC) and $I = 3.122$ THz², $\langle\omega^2\rangle = 6.411$ THz² (no SOC), thus the main reason for the increase in λ due to SOC is the decrease of the phonon frequencies. Similar integrals computed for each phonon mode are collected in Table II.

The calculated λ places ScAu₂Al in the strong coupling regime and is the largest among the values reported in Heusler compounds (YPd₂Sn has $\lambda = 0.99$ [69]). The superconducting transition temperature may now be calculated from the Allen-Dynes formula [49]:

$$k_B T_c = \frac{f_1 f_2 \hbar \omega_{\text{ln}}}{1.20} \exp \left\{ -\frac{1.04(1 + \lambda)}{\lambda - \mu^*(1 + 0.62\lambda)} \right\}. \quad (9)$$

As λ is on the order of 1.0, the strong-coupling prefactors f_1 and f_2 must be used. They are defined as [49]

$$f_1 = [1 + (\lambda/\Lambda_1)^{3/2}]^{1/3}, \quad (10)$$

$$f_2 = 1 + \frac{(\bar{\omega}_2/\omega_{\text{ln}} - 1)\lambda^2}{\lambda^2 + \Lambda_2^2}, \quad \bar{\omega}_2 = \sqrt{2\langle\omega^2\rangle}, \quad (11)$$

where

$$\Lambda_1 = 2.46(1 + 3.8\mu^*) \quad (12)$$

and

$$\Lambda_2 = 1.82(1 + 6.3\mu^*)(\bar{\omega}_2/\omega_{\text{ln}}). \quad (13)$$

The logarithmic average phonon frequency is in a form:

$$\omega_{\text{ln}} = \exp \left(\frac{2}{\lambda} \int_0^{\omega_{\text{max}}} \alpha^2 F(\omega) \ln \omega \frac{d\omega}{\omega} \right). \quad (14)$$

The calculated T_c , λ and ω_{ln} are collected in Table III. Although the phonon modes reach approximately 7.5 THz, a small $\omega_{\text{ln}} = 1.08$ THz (51.8 K, with SOC) is obtained. This is a consequence of the enhancement of the Eliashberg function in the low-frequency range, especially in the fully relativistic

case. The scalar-relativistic value of $\omega_{\text{ln}} = 1.32$ THz is 23% higher. If the phonon DOS $F(\omega)$ function was used to compute ω_{ln} value, instead of the Eliashberg function, it would be about 40% higher, 1.45 THz (69.6 K) in the relativistic case. Thus enhancement of the Eliashberg function over the phonon DOS for lower ω is responsible for such a low ω_{ln} . Strong-coupling correcting factors are $f_1 \cdot f_2 = 1.12$ (with SOC) and $f_1 \cdot f_2 = 1.08$ (without SOC). Taking the value of the Coulomb pseudopotential parameter $\mu^* = 0.10$ we obtain the critical temperature of $T_c = 5.43$ K (with SOC), which is in good agreement with the experimental one, equal to $T_c = 5.12$ K. The spin-orbit coupling increases T_c in ScAu₂Al, as the scalar-relativistic value is 4.57 K.

Although the electron-phonon coupling constant $\lambda = 1.25$ is record high in the family of Heusler compounds, the critical temperature of ScAu₂Al is not that high. The reason for this is the remarkably low $\omega_{\text{ln}} \simeq 52$ K, only 12% increased by the strong coupling correction factors $f_1 \cdot f_2 = 1.12$, when T_c is calculated. This peculiar electron-phonon spectral function, with low-frequency enhancement, together with the large value of λ is responsible for the significant underestimate of the electron-phonon coupling constant made on the basis of experimental T_c , Debye temperature ($\theta_D = 180$ K), and McMillan formula in Ref. [37]. Due to the highly non-Debye phonon spectrum and strong coupling, the McMillan formula is very inaccurate for ScAu₂Al, which explains why much smaller $\lambda = 0.77$ was obtained there.

Our calculations also demonstrate that in the Heusler family of superconductors we reach the strong-coupling regime

TABLE III. Logarithmic average ω_{ln} , electron-phonon coupling constant λ , superconducting transition temperature T_c from Allen-Dynes formula (9) with $\mu^* = 0.1$, and Sommerfeld coefficient γ renormalized with λ from the electron-phonon calculations, $\gamma = \gamma_{\text{band}}(1 + \lambda)$. Experimental value of $T_c = 5.12$ K.

	ω_{ln} (THz)	λ	T_c (K)	γ ($\frac{\text{mJ}}{\text{mol K}^2}$)
with SOC	1.077	1.253	5.43	10.68
w/o SOC	1.324	0.974	4.57	9.51

¹In a monoatomic system, the McMillan-Hopfield parameter [40] is defined as $\eta = 2MI$ (M is the atomic mass) and then the electron-phonon coupling constant is calculated using the well-known formula $\lambda = \frac{\eta}{M\langle\omega^2\rangle}$.

with $\lambda > 1$ in the compound with the highest T_c , like in the other intermetallic families of superconductors.

D. Superconductivity from the SCDFT

The motivations for extending our calculations and applying the density functional theory for superconductors method (SCDFT) to ScAu_2Al were threefold. First, we avoid using the arbitrary value of the Coulomb pseudopotential μ^* , as in the SCTK package [47] Coulomb interactions are directly included in the calculations. This allows us to verify whether the computed strong electron-phonon coupling indeed leads to a critical temperature value of the order of 5 K, with no external parameters. Second, SCDFT calculations allow us to investigate the superconducting gap structure in the reciprocal space. This is especially interesting as ScAu_2Al occurred to be a two-band material, with two large Fermi surface sheets. Therefore it is possible that different strengths of the electron-phonon interaction on those two sheets will lead to the formation of two different superconducting gaps, as is observed, e.g., in Pb [70]. Two-gap superconductivity was recently suggested in a noncentrosymmetric half-Heusler compound LuPdBi [71] based on upper critical field and penetration depth measurements.

Third, in the experimental studies [37] a quadratic temperature dependence of resistivity, $\rho(T) = \rho_0 + AT^2$ was observed. Such a quadratic temperature dependence may be induced by the presence of weak ferromagnetic spin fluctuations (SF), which would additionally compete with superconductivity. The presence of SF may be taken into account in SCDFT calculations within SCTK thus we aimed to verify whether SF have a strong influence on superconductivity in ScAu_2Al . All calculations reported in this section include the spin-orbit coupling.

The superconductivity in SCTK is described with the equation for the superconducting gap function $\Delta_{n\mathbf{k}}$:

$$\Delta_{n\mathbf{k}} = -\frac{1}{2} \sum_{n'\mathbf{k}'} \frac{K_{n\mathbf{k}n'\mathbf{k}'}(\xi_{n\mathbf{k}}, \xi_{n'\mathbf{k}'})}{1 + Z_{n\mathbf{k}}(\xi_{n\mathbf{k}})} \times \frac{\Delta_{n'\mathbf{k}'}}{\sqrt{\xi_{n'\mathbf{k}'}^2 + \Delta_{n'\mathbf{k}'}^2}} \tanh \frac{\sqrt{\xi_{n'\mathbf{k}'}^2 + \Delta_{n'\mathbf{k}'}^2}}{2T}, \quad (15)$$

where $\xi_{n\mathbf{k}}$ is the Kohn-Sham eigenvalue at $E_F = 0$ in the band n . T_c is found when the gap vanishes at a given temperature. The integration kernel K

$$K_{n\mathbf{k}n'\mathbf{k}'}(\xi, \xi') \equiv K_{n\mathbf{k}n'\mathbf{k}'}^{ep}(\xi, \xi') + K_{n\mathbf{k}n'\mathbf{k}'}^{ee}(\xi, \xi') + K_{n\mathbf{k}n'\mathbf{k}'}^{sf}(\xi, \xi') \quad (16)$$

consist of electron-phonon, electron-electron and spin fluctuations terms. The renormalization factor Z :

$$Z_{n\mathbf{k}}(\xi) = Z_{n\mathbf{k}}^{ep}(\xi) + Z_{n\mathbf{k}}^{sf}(\xi) \quad (17)$$

has only the electron-phonon and SF terms. The screened Coulomb interaction is calculated with the random phase approximation. A more detailed description of the theory can be found in [47,48].

We first discuss the results of calculations with the spin fluctuation terms neglected. The main results of the calcu-

TABLE IV. Results of SCDFT calculations in a form of average parameters for FS sheets corresponding to band 1, band 2, and the global average, obtained with and without spin fluctuations (all with spin-orbit coupling): μ -Coulomb repulsion parameter, Δ -superconducting gap, λ -electron-phonon coupling constant. T_c is the superconducting critical temperature.

	w/o SF	with SF
$\bar{\mu}_{b_1}$	0.270	0.297
$\bar{\mu}_{b_2}$	0.273	0.298
$\bar{\mu}$	0.271	0.297
$\bar{\Delta}_{b_1}$ (meV)	0.909	0.840
$\bar{\Delta}_{b_2}$ (meV)	0.947	0.878
$\bar{\Delta}$ (meV)	0.921	0.854
$2\bar{\Delta}_{b_1}/k_B T_c$	4.093	4.075
$2\bar{\Delta}_{b_2}/k_B T_c$	4.273	4.264
$2\bar{\Delta}/k_B T_c$	4.138	4.119
$\bar{\lambda}_{b_1}$	1.355	1.355
$\bar{\lambda}_{b_2}$	1.387	1.387
$\bar{\lambda}$	1.364	1.364
T_c (K)	5.16	4.79

lations are shown in Table IV. The superconducting critical temperature, calculated from SCDFT based on the gap equation (15) and the condition of vanishing gap at the transition point, is $T_c = 5.16$ K. This value is almost identical to $T_c = 5.12$ K, reported in the experiment in Ref. [37], and larger than $T_c = 4.4$ K previously reported for that system [29,38]. This confirms that ScAu_2Al has intrinsically the highest critical temperature among the Heusler compounds studied so far, and the lower value, reported in earlier studies [38], may be due to disorder in the samples.

Figure 12 presents the \mathbf{k} -space distribution of the key parameters for the superconductivity of ScAu_2Al : the value of the electron-phonon coupling parameter $\lambda_{n\mathbf{k}}$ in panel (a), the screened Coulomb repulsion parameter $\mu_{n\mathbf{k}}$ in panel (b), and the wave-vector dependence of the superconducting gap $\Delta_{n\mathbf{k}}$ in panel (c), each plotted on the Fermi surface of the compound. Panels (d)–(f) show those quantities in a form of histograms.

First of all, superconductivity is fully gaped, there are no points or lines with nodes. A moderate level of anisotropy and a quite large spread of the discussed quantities is observed, more pronounced for the Fermi surface associated with the first band. The electron-phonon coupling parameter $\lambda_{n\mathbf{k}}$ takes values between 0.7 and 2.0, and the regions with stronger coupling also have weaker screened electron repulsion parameter $\mu_{n\mathbf{k}}$. This results in a distribution of $\Delta_{n\mathbf{k}}$ with quite a noticeable spread, the ratio of the highest to the lowest values reaches about 2. Most of the FS regions exhibit $4 < 2\Delta/k_B T_c < 5$, much above the BCS weak-coupling limit of 3.53. The regions with the strongest electron-phonon coupling, which includes the nested parts of the FS according to Fig. 8, correspond to the largest $\Delta_{n\mathbf{k}}$. For example, the gap in the Γ - K direction, where the acoustic phonon modes are strongly coupled and the nesting function is enhanced, has a higher value than in Γ - L . The gap near the L point has moderate values, as well as relatively small phonon linewidths

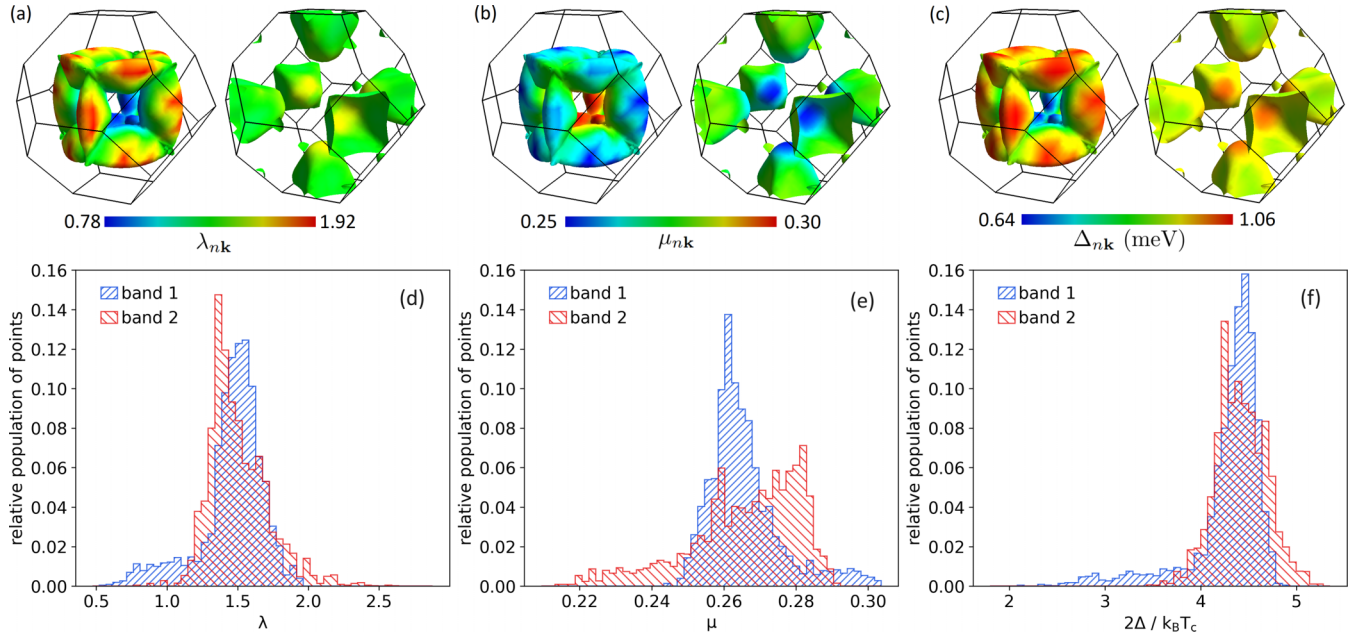


FIG. 12. The $n\mathbf{k}$ dependent (a) electron-phonon coupling constant, (b) Coulomb potential and (c) superconducting gap function at $T = 0$ K. Histograms in (d), (e), and (f) present the distribution of the quantities that were plotted on the Fermi surface. These results were computed with SOC and w/o SF.

seen in Fig. 10, which shows that the flat band at L does not affect the superconductivity much.

From the k -dependent values, we calculate the average superconducting gaps for each band, by weighting $\Delta_{n\mathbf{k}}$ by the k -resolved density of states at E_F

$$\bar{\Delta}_n = \frac{\sum_{\mathbf{k}} \Delta_{n\mathbf{k}} \delta(E_{\mathbf{k}} - E_F)}{\sum_{\mathbf{k}} \delta(E_{\mathbf{k}} - E_F)}. \quad (18)$$

The $\delta(E_{\mathbf{k}} - E_F)$ functions are computed using the Marzari-Vanderbilt cold smearing method [72,73], more details are given in Ref. [55]. The average Coulomb repulsion parameters $\bar{\mu}_n$ and electron-phonon coupling constants $\bar{\lambda}_n$ were computed in the same way, and $n = \{b_1, b_2\}$ stand for the Fermi surface sheet of band 1 and band 2. The global averages are also computed by weighting each FS sheet contribution. The results are collected in Table IV. The average values of the superconducting gaps confirm the strong-coupling character of superconductivity in ScAu₂Al, as $2\bar{\Delta}_{b_1}/k_B T_c = 4.09$ and $2\bar{\Delta}_{b_2}/k_B T_c = 4.27$, both considerably above the BCS value. As the first FS sheet contributes about 75% to $N(E_F)$ due to lower Fermi velocities (see Fig. 2), the global average is closer to the Δ_{b_1} , with $2\bar{\Delta}/k_B T_c = 4.14$. The Fermi surface average electron-phonon coupling parameters $\bar{\lambda}_n$ are similar for both FS sheets, and the global average $\bar{\lambda} = 1.36$. This value is 9% larger than the value computed from the Eliashberg function in the previous section ($\lambda = 1.25$). The difference is the result of different numerical procedures of calculations of λ for the two cases, including unshifted vs. shifted \mathbf{q} -point meshes or smearing vs. tetrahedron integration methods. Nevertheless, the difference is not significant and even stronger electron-phonon coupling is predicted by the SCDFT calculations.

The screened Coulomb interaction parameter $\mu_{n\mathbf{k}}$ is shown in Fig. 12(b). It is obtained from the electron-electron part of the kernel $K_{n\mathbf{k}n'\mathbf{k}'}$ [see Eq. (16)] by summing over $\{n'\mathbf{k}'\}$ on the

Fermi surface. By integrating it again, one obtains the average Coulomb repulsion parameter $\bar{\mu}$, shown in Table IV, which is a dimensionless product of the average interaction kernel times the density of states at E_F [48]. Both FS sheets have similar values, and the overall average is $\bar{\mu} = 0.27$. Compared to elemental metals that build our structure, Au with the filled d shell well below the Fermi energy has a lower $\bar{\mu} = 0.14$, metallic Al has a similar $\bar{\mu} = 0.25$ and Sc with an open $3d$ shell has a much higher $\bar{\mu} = 0.52$ [48].

In the superconducting state, the effect of Coulomb repulsive interactions is weakened by retardation effects due to different energy scales of electrons and phonons, and this effect is naturally included in the SCDFT calculations [48]. In the isotropic Eliashberg theory or in the Allen-Dynes formula, retardation is approximately described using the μ^* parameter [74–78]

$$\mu^* = \frac{\mu}{1 + \mu \ln(E_{\text{el}}/\omega_{\text{ph}})}. \quad (19)$$

The E_{el} and ω_{ph} are usually taken as the electronic and phononic cutoff energies, of the order of Fermi energy or bandwidth for the former and ω_{max} or θ_D for the latter (due to the logarithm in the denominator the slightly different definitions do not affect μ^* much). Based on the calculated $\bar{\mu}$ we may estimate μ^* . With an electronic bandwidth of 10 eV and a maximum phonon frequency of 7.5 THz (31 meV) one obtains $\mu^* = 0.105$. If the Debye temperature of 180 K is used, instead of ω_{max} , a smaller $\mu^* = 0.092$ is obtained, but all close to the standard approximation of $\mu^* = 0.10$.

Now, let us proceed to the analysis of the spin fluctuation effect. Figure 13(a) shows the \mathbf{k} -space distribution of the repulsion parameter $\mu_{n\mathbf{k}}$, which now includes both the Coulomb and spin-fluctuation kernels. In panel (b) the superconducting gap is presented, and panels (c) and (d) show

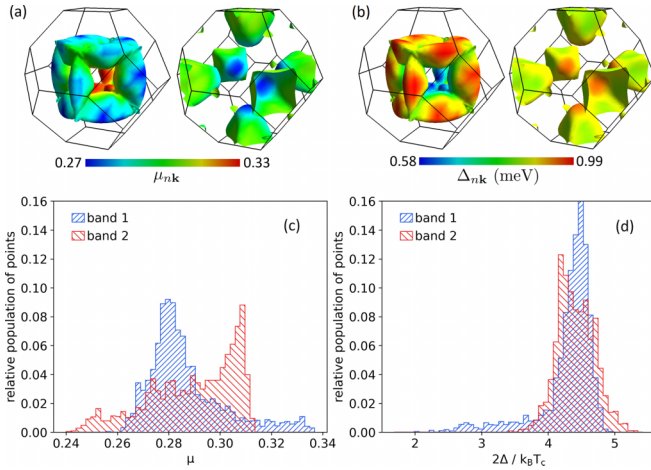


FIG. 13. The nk dependent (a) Coulomb potential and (b) superconducting gap function at $T = 0$ K. Histograms in (c) and (d) present the distribution of the quantities that were plotted on the Fermi surface. These results were computed with SOC and SF.

their histograms. SF term does not influence λ_{nk} , so it is not repeated after Fig. 12. The critical temperature drops a little, to $T_c = 4.79$ K, now slightly lower than the experimental result of 5.12 K in Bag *et al.* [37], yet still larger than 4.4 K in an earlier report [38]. The repulsion parameter μ_{nk} increases, its \mathbf{k} -dependence becomes a bimodal distribution, with peaks in the histograms shifted between the two bands. Nevertheless the average values for the two FS sheets become equal (see Table IV) and increase in about 10% due to SF to $\bar{\mu} = 0.30$.² In elemental metallic scandium, where strong spin fluctuations are present, the SF contribution to the repulsion parameter is much larger, $\bar{\mu}_{SF} = 0.976$ [48], which makes the compound nonsuperconducting. The small increase in $\bar{\mu}$ in ScAu₂Al is responsible for the small decrease in T_c and in the superconducting gaps, compared to the no-SF calculations; however, the ratios $2\Delta_n/k_B T_c$ remain practically unchanged. From our calculations, we may conclude that the spin fluctuations are weak in ScAu₂Al.

In the final step of our analysis of the superconducting properties of ScAu₂Al, we have calculated the temperature-dependent quasiparticle density of states in a superconducting phase (see Ref. [47] for details) and the temperature evolution of the superconducting gap. Figure 14 shows the quasiparticle DOS spectrum for 0.1, 2, and 4 K, computed with and without spin fluctuations (both include SOC). As one can clearly see, it deviates from the BCS-like singularity at the energy gap and it is a consequence of the \mathbf{k} dependence and energy spread of the superconducting gaps, discussed above. The small hump at its beginning comes from the “tail” seen on Δ_{nk} histograms in Figs. 12 and 13. Tunneling conductance measurements should be performed to verify our calculations and further investigate the gap anisotropy. Figure 15 presents the temperature dependence of the average value of superconducting gaps for bands

²If we would like to compare the effective μ^* parameter including the retardation effects, Eq. (19), the increase of μ^* due to SF is about 5%.

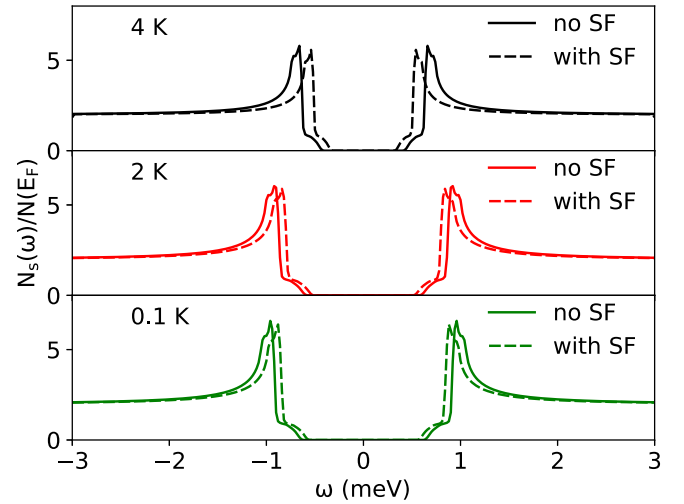


FIG. 14. Quasiparticle spectrum as a function of temperature. Its shape is visibly affected by the anisotropy of the superconducting gap.

1 and 2, computed with and without SF (both include SOC). The gaps were fitted to the equation:

$$\Delta(T) = \Delta(0) \sqrt{1 - \left(\frac{T}{T_c}\right)^n}, \quad (20)$$

where in the BCS model $n \simeq 3.0$ [79]. Here, the fitting gives a smaller exponent of $n \simeq 2.5$ with SF and $n \simeq 2.6$ without SF.

IV. SUMMARY

To summarize, we have presented calculations of the electronic structure, phonons, electron-phonon coupling functions, superconducting critical temperature, and superconducting gap in ScAu₂Al. Spin-orbit coupling is found to have an important effect on the electronic structure near the Fermi level, because it lifts the degeneracy of the bands, removing

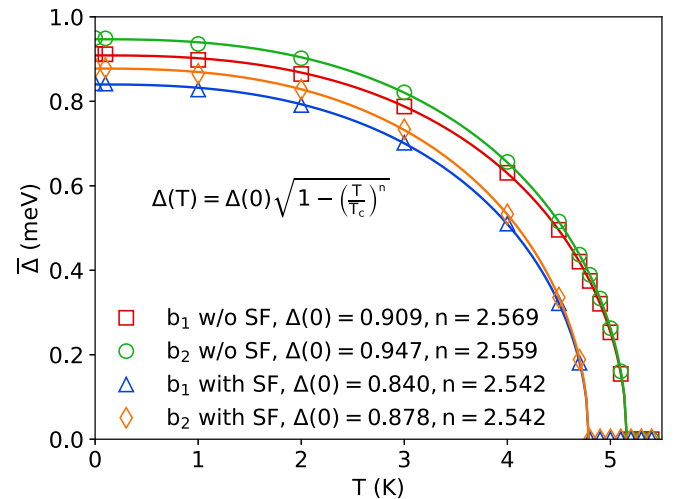


FIG. 15. Temperature dependence of the average values of superconducting gaps, calculated without and with spin fluctuations. Lines are fits to the formula (20).

the van Hove singularity from the vicinity of the Fermi level. Sc-*d* states contribute approximately 50% of the density of states at the Fermi level, while the Al-*p* states contribute 30% with Au-*d* and Au-*s* constituting the rest. Due to a large difference of the Au atom mass compared to Sc and Al, phonons form two groups of modes, separated by a large gap of approximately 2 THz. Although Sc is heavier than Al, phonon modes dominated by its vibrations have higher frequencies due to the stronger bonding of Sc in the structure. The most important feature of the phonon structure to provide the strong electron-phonon coupling in this compound is a low-dispersive acoustic branch in the Γ -X direction that has significantly lower frequencies than the rest of the spectrum and is dominated by Au vibrations. The SOC further softens phonons in that branch, resulting in a large value of the electron-phonon coupling constant $\lambda = 1.25$. Therefore ScAu₂Al can be classified as a strong coupling superconductor. Using the Allen-Dynes formula with strong coupling correction factors, we obtained $T_c = 5.43$ K when using a typical value of $\mu^* = 0.10$.

These conclusions are then strengthened by the SCDFD calculations, in which the depairing effects of Coulomb interactions and spin fluctuations are taken into account. The average electron-phonon coupling parameter, obtained for SCDFD calculations, confirmed that the coupling is strong, giving a slightly larger $\lambda = 1.36$. If SF are neglected, the

critical temperature of $T_c = 5.16$ K is obtained, and the inclusion of SF slightly decreases the critical temperature to $T_c = 4.79$ K. The obtained T_c is close to the experimental one of 5.12 K, confirming the electron-phonon coupling mechanism of superconductivity in ScAu₂Al and showing that spin fluctuations are weak. Analysis of the Fermi surface and superconducting gaps show that ScAu₂Al is a two-band superconductor with nodeless gaps and a moderate level of gap anisotropy. The values of $2\Delta/k_B T_c$ are 4.09 and 4.27 for the two Fermi surface sheets, above the weak coupling limit of 3.53. The calculated quasiparticle density of states is strongly affected by the large spread of superconducting energy gap values and its anisotropy, opening a possibility of its experimental validation through the tunneling spectroscopy measurements.

ACKNOWLEDGMENTS

This work was supported by the National Science Centre (Poland), Project No. 2017/26/E/ST3/00119. We gratefully acknowledge Polish high-performance computing infrastructure PLGrid (HPC Centers: ACK Cyfronet AGH) for providing computer facilities and support within computational Grants No. PLG/2022/015620 and No. PLG/2023/016451. We thank Kamil Kutorasiński for help in evaluating the nesting function.

-
- [1] X.-Q. Chen, R. Podloucky, and P. Rogl, *Ab initio* prediction of half-metallic properties for the ferromagnetic Heusler alloys Co₂MSi (M=Ti,V,Cr), *J. Appl. Phys.* **100**, 113901 (2006).
- [2] N. I. Kourov, V. V. Marchenkov, A. V. Korolev, L. A. Stashkova, S. M. Emel'yanova, and H. W. Weber, Specific features of the properties of half-metallic ferromagnetic Heusler alloys Fe₂MnAl, Fe₂MnSi, and Co₂MnAl, *Phys. Solid State* **57**, 700 (2015).
- [3] M. Mouatassime, Y. Selmani, S. Idrissi, L. Bahmad, F. Goumrhar, H. Labrim, and A. Benyoussef, Magnetic properties and half metallic behavior of the Full-Heusler Co₂FeGe alloy: DFT and Monte Carlo studies, *J. Solid State Chem.* **304**, 122534 (2021).
- [4] R. Shan, H. Sukegawa, W. H. Wang, M. Kodzuka, T. Furubayashi, T. Ohkubo, S. Mitani, K. Inomata, and K. Hono, Demonstration of half-metallicity in Fermi-level-tuned Heusler alloy Co₂FeAl_{0.5}Si_{0.5} at room temperature, *Phys. Rev. Lett.* **102**, 246601 (2009).
- [5] C. Felser, L. Wollmann, S. Chadov, G. H. Fecher, and S. S. P. Parkin, Basics and prospective of magnetic Heusler compounds, *APL Mater.* **3**, 041518 (2015).
- [6] T. Graf, S. S. P. Parkin, and C. Felser, Heusler compounds—A material class with exceptional properties, *IEEE Trans. Magn.* **47**, 367 (2011).
- [7] S. Idrissi, H. Labrim, S. Ziti, and L. Bahmad, Investigation of the physical properties of the equiatomic quaternary Heusler alloy CoYCrZ (Z = Si and Ge): a DFT study, *Appl. Phys. A* **126**, 190 (2020).
- [8] S. Idrissi, H. Labrim, S. Ziti, and L. Bahmad, Characterization of the equiatomic quaternary Heusler alloy ZnCdRhMn: Structural, electronic, and magnetic properties, *J. Supercond. Nov. Magn.* **33**, 3087 (2020).
- [9] S. Idrissi, H. Labrim, S. Ziti, and L. Bahmad, Structural, electronic, magnetic properties and critical behavior of the equiatomic quaternary Heusler alloy CoFeTiSn, *Phys. Lett. A* **384**, 126453 (2020).
- [10] S. Idrissi, S. Ziti, H. Labrim, and L. Bahmad, Half-metallicity and magnetism in the full Heusler alloy Fe₂MnSn with L21 and XA stability ordering phases, *J. Low Temp. Phys.* **202**, 343 (2021).
- [11] Z. H. Liu, M. Zhang, Y. T. Cui, Y. Q. Zhou, W. H. Wang, G. H. Wu, X. X. Zhang, and Xiao Gang, Martensitic transformation and shape memory effect in ferromagnetic Heusler alloy Ni₂FeGa, *Appl. Phys. Lett.* **82**, 424 (2003).
- [12] M. Acet and E. F. Wassermann, Magnetic interactions in Ni-Mn-based magnetic shape-memory Heusler alloys, *Adv. Eng. Mater.* **14**, 523 (2012).
- [13] S. Takayanagi, S. B. Woods, N. Wada, T. Watanabe, Y. Onuki, A. Kobori, T. Komatsubara, M. Imai, and H. Asano, Magnetic and transport properties in the cubic heavy fermion system CeInCu₂, *J. Magn. Magn. Mater.* **76-77**, 281 (1988).
- [14] R. Lahiouel, J. Pierre, E. Siaud, R. M. Galera, M. J. Besnus, J. P. Kappler, and A. P. Murani, Kondo lattice and heavy fermions in Heusler phases: CeInAg_{2-x}Cu_x, *Z. Phys. B* **67**, 185 (1987).
- [15] H. Nakamura, Y. Kitaoka, K. Asayama, Y. Onuki, and T. Komatsubara, Observation of two phase transitions in the Heusler heavy fermion system CeInCu₂, *J. Magn. Magn. Mater.* **76-77**, 467 (1988).
- [16] D. Kaczorowski, A. Leithe-Jasper, T. Cichorek, K. Tenya, J. Custers, P. Gegenwart, and Y. Grin, Possible heavy-fermion

- behavior in a Heusler-type compound YbPd₂Sb, *Acta Phys. Pol. B* **34**, 1253 (2003).
- [17] K. Gofryk, D. Kaczorowski, T. Plackowski, A. Leithe-Jasper, and Yu. Grin, Magnetic and transport properties of the rare-earth-based Heusler phases RPdZ and RPd₂Z (Z=Sb,Bi), *Phys. Rev. B* **72**, 094409 (2005).
- [18] T. Gruner, D. Jang, Z. Huesges, R. Cardoso-Gil, G. H. Fecher, M. M. Koza, O. Stockert, A. P. Mackenzie, M. Brando, and C. Geibel, Charge density wave quantum critical point with strong enhancement of superconductivity, *Nat. Phys.* **13**, 967 (2017).
- [19] W. Al-Sawai, H. Lin, R. S. Markiewicz, L. A. Wray, Y. Xia, S.-Y. Xu, M. Z. Hasan, and A. Bansil, Topological electronic structure in half-Heusler topological insulators, *Phys. Rev. B* **82**, 125208 (2010).
- [20] Z. K. Liu, L. X. Yang, S.-C. Wu, C. Shekhar, J. Jiang, H. F. Yang, Y. Zhang, S.-K. Mo, Z. Hussain, B. Yan, C. Felser, and Y. L. Chen, Observation of unusual topological surface states in half-Heusler compounds LnPtBi (Ln=Lu, Y), *Nat. Commun.* **7**, 12924 (2016).
- [21] Y. Sun and C. Felser, *Topological Matter Lectures from the Topological Matter School 2017* (Springer Nature, Cham, Switzerland, 2018), pp. 199–210.
- [22] O. Pavlosiuk, D. Kaczorowski, X. Fabreges, A. Gukasov, and P. Wisniewski, Antiferromagnetism and superconductivity in the half-Heusler semimetal HoPdBi, *Sci. Rep.* **6**, 18797 (2016).
- [23] P.-J. Guo, H.-C. Yang, K. Liu, and Z.-Y. Lu, Type-II Dirac semimetals in the YPd₂Sn class, *Phys. Rev. B* **95**, 155112 (2017).
- [24] J. H. Wernick, G. W. Hull, T. H. Geballe, J. E. Bernardini, and J. V. Waszczak, Superconductivity in ternary Heusler intermetallic compounds, *Mater. Lett.* **2**, 90 (1983).
- [25] T. Klimczuk, C. H. Wang, K. Gofryk, F. Ronning, J. Winterlik, G. H. Fecher, J.-C. Griveau, E. Colineau, C. Felser, J. D. Thompson, D. J. Safarik, and R. J. Cava, Superconductivity in the Heusler family of intermetallics, *Phys. Rev. B* **85**, 174505 (2012).
- [26] O. Pavlosiuk, D. Kaczorowski, and P. Wiśniewski, Superconductivity and Shubnikov–de Haas oscillations in the noncentrosymmetric half-Heusler compound YPtBi, *Phys. Rev. B* **94**, 035130 (2016).
- [27] O. Pavlosiuk, D. Kaczorowski, and P. Wiśniewski, Shubnikov - de Haas oscillations, weak antilocalization effect and large linear magnetoresistance in the putative topological superconductor LuPdBi, *Sci. Rep.* **5**, 9158 (2015).
- [28] J. Winterlik, G. H. Fecher, A. Thomas, and C. Felser, Superconductivity in palladium-based Heusler compounds, *Phys. Rev. B* **79**, 064508 (2009).
- [29] M. J. Winiarski, G. Kuderowicz, K. Górnicka, L. S. Litzbarski, K. Stolecka, B. Wiendlocha, R. J. Cava, and T. Klimczuk, MgPd₂Sb: A Mg-based Heusler-type superconductor, *Phys. Rev. B* **103**, 214501 (2021).
- [30] L. Wollmann, A. K. Nayak, S. S. P. Parkin, and C. Felser, Heusler 4.0: Tunable Materials, *Annu. Rev. Mater. Res.* **47**, 247 (2017).
- [31] V. Aljani, J. Winterlik, G. H. Fecher, and C. Felser, Tuning the magnetism of the Heusler alloys Mn_{3-x}Co_xGa from soft and half-metallic to hard-magnetic for spin-transfer torque applications, *Appl. Phys. Lett.* **99**, 222510 (2011).
- [32] T. Graf, C. Felser, and S. S. P. Parkin, Simple rules for the understanding of Heusler compounds, *Prog. Solid State Chem.* **39**, 1 (2011).
- [33] N. Fukatani, K. Ueda, and H. Asano, Epitaxial strain and antiferromagnetism in Heusler Fe₂VSi thin films, *J. Appl. Phys.* **109**, 073911 (2011).
- [34] X. T. Wang, Z. X. Cheng, J. L. Wang, H. Rozale, L. Y. Wang, Z. Y. Yu, J. T. Yang, and G. D. Liu, Strain-induced diverse transitions in physical nature in the newly designed inverse Heusler alloy Zr₂MnAl, *J. Alloys Compd.* **686**, 549 (2016).
- [35] B. T. Matthias, Transition temperatures of superconductors, *Phys. Rev.* **92**, 874 (1953).
- [36] B. T. Matthias, Empirical relation between superconductivity and the number of valence electrons per atom, *Phys. Rev.* **97**, 74 (1955).
- [37] B. Bag, R. Loke, B. Singh, A. Thamizhavel, B. Singh, and S. Ramakrishnan, Superconductivity in Heusler compound ScAu₂Al, *J. Phys.: Condens. Matter* **34**, 195403 (2022).
- [38] C. P. Poole Jr., P. C. Canfield, and A. P. Ramirez, in *Handbook of Superconductivity*, edited by C. P. Poole Jr. (Academic Press, New York, 2000), Chap. 5.
- [39] C. Benndorf, O. Niehaus, H. Eckert, and O. Janka, ²⁷Al and ⁴⁵Sc NMR spectroscopy on ScT₂Al and Sc(T_{0.5}T'_{0.5})₂Al (T = T' = Ni, Pd, Pt, Cu, Ag, Au) Heusler phases and superconductivity in Sc(Pd_{0.5}Au_{0.5})₂Al, *Z. Anorg. Allg. Chem.* **641**, 168 (2015).
- [40] W. L. McMillan, Transition temperature of strong-coupled superconductors, *Phys. Rev.* **167**, 331 (1968).
- [41] S. Gutowska, K. Górnicka, P. Wójcik, T. Klimczuk, and B. Wiendlocha, Strong-coupling superconductivity of SrIr₂ and SrRh₂: Phonon engineering of metallic Ir and Rh, *Phys. Rev. B* **104**, 054505 (2021).
- [42] N. Haldolaarachchige, Q. Gibson, L. M. Schoop, H. Luo, and R. J. Cava, Characterization of the heavy metal pyrochlore lattice superconductor CaIr₂, *J. Phys.: Condens. Matter* **27**, 185701 (2015).
- [43] H. M. Tütüncü, H. Y. Uzunok, E. Karaca, E. Arslan, and G. P. Srivastava, Effects of spin-orbit coupling on the electron-phonon superconductivity in the cubic Laves-phase compounds CaIr₂ and CaRh₂, *Phys. Rev. B* **96**, 134514 (2017).
- [44] G. R. Stewart, Superconductivity in the A15 structure, *Phys. C Supercond. Appl.* **514**, 28 (2015).
- [45] L. N. Oliveira, E. K. U. Gross, and W. Kohn, Density-functional theory for superconductors, *Phys. Rev. Lett.* **60**, 2430 (1988).
- [46] M. Lüders, M. A. L. Marques, N. N. Lathiotakis, A. Floris, G. Profeta, L. Fast, A. Continenza, S. Massidda, and E. K. U. Gross, *Ab initio* theory of superconductivity. I. Density functional formalism and approximate functionals, *Phys. Rev. B* **72**, 024545 (2005).
- [47] M. Kawamura, R. Akashi, and S. Tsuneyuki, Anisotropic superconducting gaps in YNi₂B₂C: A first-principles investigation, *Phys. Rev. B* **95**, 054506 (2017).
- [48] M. Kawamura, Y. Hizume, and T. Ozaki, Benchmark of density functional theory for superconductors in elemental materials, *Phys. Rev. B* **101**, 134511 (2020).
- [49] P. B. Allen and R. C. Dynes, Transition temperature of strong-coupled superconductors reanalyzed, *Phys. Rev. B* **12**, 905 (1975).
- [50] P. Giannozzi, S. Baroni, N. Bonini, M. Calandra, R. Car, C. Cavazzoni, D. Ceresoli, G. L. Chiarotti, M. Cococcioni, I.

- Dabo, A. D. Corso, S. de Gironcoli, S. Fabris, G. Fratesi, R. Gebauer, U. Gerstmann, C. Gougoussis, A. Kokalj, M. Lazzeri, L. Martin-Samos *et al.*, QUANTUM ESPRESSO: a modular and open-source software project for quantum simulations of materials, *J. Phys.: Condens. Matter* **21**, 395502 (2009).
- [51] P. Giannozzi, Jr, O. Andreussi, T. Brumme, O. Bunau, M. Buongiorno Nardelli, M. Calandra, R. Car, C. Cavazzoni, D. Ceresoli, M. Cococcioni, N. Colonna, I. Carnimeo, A. D. Corso, S. de Gironcoli, P. Delugas, R. A. DiStasio, Jr, A. Ferretti, A. Floris, G. Fratesi, G. Fugallo *et al.*, Advanced capabilities for materials modelling with quantum espresso, *J. Phys.: Condens. Matter* **29**, 465901 (2017).
- [52] A. D. Corso, Pseudopotentials periodic table: From H to Pu, *Comput. Mater. Sci.* **95**, 337 (2014).
- [53] Pseudopotential files: Sc.pbe-spn-kjpaw_psl.1.0.0.UPF, Au.pbe-spn-kjpaw_psl.1.0.0.UPF, Al.pbe-n-kjpaw_psl.1.0.0.UPF.
- [54] J. P. Perdew, K. Burke, and M. Ernzerhof, Generalized gradient approximation made simple, *Phys. Rev. Lett.* **77**, 3865 (1996).
- [55] See Supplemental Material at <http://link.aps.org/supplemental/10.1103/PhysRevB.108.224501> for Fig. S1 which compares the electronic structure obtained in pseudopotential and all-electron calculations; Fig. S2 of the phonon dispersion relations and phonon densities of states obtained on 6^3 and 8^3q -point grids with discussion of the convergence tests for λ ; Discussion of the specific heat with Fig. S3 of the Sommerfeld coefficient and Debye temperature obtained by fitting the experimental specific heat data in a various temperature range, as well as Figs. S4–S6 that demonstrate the inapplicability of the Debye model for a description of the lattice specific heat above 2 K; Additional details of the cold smearing method; Video files with the animations of atomic vibrations in the selected phonon modes.
- [56] P. Blaha, K. Schwarz, G. K. H. Madsen, D. Kvasnicka, J. Luitz, R. Laskowski, F. Tran, and L. D. Marks, *WIEN2k, An Augmented Plane Wave + Local Orbitals Program for Calculating Crystal Properties* (Karlheinz Schwarz, Vienna University of Technology, Austria) (2018).
- [57] P. Blaha, K. Schwarz, F. Tran, R. Laskowski, G. K. H. Madsen, and L. D. Marks, WIEN2k: An APW+lo program for calculating the properties of solids, *J. Chem. Phys.* **152**, 074101 (2020).
- [58] M. Kawamura, FermiSurfer: Fermi-surface viewer providing multiple representation schemes, *Comput. Phys. Commun.* **239**, 197 (2019).
- [59] P. V. Sreenivasa Reddy, G. Vaitheeswaran, and V. Kanchana, Fermi surface study of ScAu₂(Al, In) and ScPd₂(Sn, Pb) compounds, *AIP Conf. Proc.* **1665**, 090035 (2015).
- [60] A. Kokalj, XCrySDen—a new program for displaying crystalline structures and electron densities, *J. Mol. Graphics Modell.* **17**, 176 (1999).
- [61] L. Zhang and Q. Niu, Chiral phonons at high-symmetry points in monolayer hexagonal lattices, *Phys. Rev. Lett.* **115**, 115502 (2015).
- [62] J. Skórka, K. J. Kapcia, P. T. Jochym, and A. Ptok, Chiral phonons in binary compounds ABi (A = K, Rb, Cs) with P21/c structure, *Mater. Today Commun.* **35**, 105888 (2023).
- [63] S. Basak, P. Piekarczyk, and A. Ptok, Chiral phonon in the cubic system based on the Laves phase of ABi₂ (A = K, Rb, Cs), *Comput. Mater. Sci.* **230**, 112545 (2023).
- [64] G. Grimvall, *The Electron-Phonon Interaction in Metals* (North-Holland, Amsterdam, 1981).
- [65] F. Giustino, Electron-phonon interactions from first principles, *Rev. Mod. Phys.* **89**, 015003 (2017).
- [66] M. Wierzbowska, S. de Gironcoli, and P. Giannozzi, Origins of low- and high-pressure discontinuities of T_c in niobium, [arXiv:cond-mat/0504077](https://arxiv.org/abs/cond-mat/0504077).
- [67] P. B. Allen, Neutron spectroscopy of superconductors, *Phys. Rev. B* **6**, 2577 (1972).
- [68] G. Kuderowicz, P. Wójcik, and B. Wiendlocha, Pressure effects on the electronic structure, phonons, and superconductivity of noncentrosymmetric ThCoC₂, *Phys. Rev. B* **105**, 214528 (2022).
- [69] H. M. Tutuncu and G. P. Srivastava, Phonon anomalies and superconductivity in the Heusler compound YPd₂Sn, *J. Appl. Phys.* **116**, 013907 (2014).
- [70] M. Ruby, B. W. Heinrich, J. I. Pascual, and K. J. Franke, Experimental demonstration of a two-band superconducting state for lead using scanning tunneling spectroscopy, *Phys. Rev. Lett.* **114**, 157001 (2015).
- [71] K. Ishihara, T. Takenaka, Y. Miao, Y. Mizukami, K. Hashimoto, M. Yamashita, M. Konczykowski, R. Masuki, M. Hirayama, T. Nomoto, R. Arita, O. Pavlosiuk, P. Wiśniewski, D. Kaczorowski, and T. Shibauchi, Tuning the parity mixing of singlet-septet pairing in a half-Heusler superconductor, *Phys. Rev. X* **11**, 041048 (2021).
- [72] N. Marzari, D. Vanderbilt, A. De Vita, and M. C. Payne, Thermal contraction and disordering of the Al(110) surface, *Phys. Rev. Lett.* **82**, 3296 (1999).
- [73] F. J. dos Santos and N. Marzari, Fermi energy determination for advanced smearing techniques, *Phys. Rev. B* **107**, 195122 (2023).
- [74] N. N. Bogoljubov, On a new method in the theory of superconductivity, *Il Nuovo Cimento* **7**, 794 (1958).
- [75] P. Morel and P. W. Anderson, Calculation of the superconducting state parameters with retarded electron-phonon interaction, *Phys. Rev.* **125**, 1263 (1962).
- [76] J. P. Carbotte, Properties of boson-exchange superconductors, *Rev. Mod. Phys.* **62**, 1027 (1990).
- [77] K.-H. Lee and K. J. Chang, Linear-response calculation of the Coulomb pseudopotential μ^* for Nb, *Phys. Rev. B* **54**, 1419 (1996).
- [78] J. Bauer, J. E. Han, and O. Gunnarsson, Retardation effects and the Coulomb pseudopotential in the theory of superconductivity, *Phys. Rev. B* **87**, 054507 (2013).
- [79] G. Kuderowicz, P. Wójcik, and B. Wiendlocha, Electronic structure, electron-phonon coupling, and superconductivity in noncentrosymmetric ThCoC₂ from *ab initio* calculations, *Phys. Rev. B* **104**, 094502 (2021).